photonics

MDPI

Article

Engineering of TiO_2 or ZnO—Graphene Oxide Nanoheterojunctions for Hybrid Solar Cells Devices

Duarte Carreira [1], Paulo A. Ribeiro [2], Maria Raposo [2] and Susana Sério [2,*]

[1] Departamento de Física, Faculdade de Ciências e Tecnologia, Universidade NOVA de Lisboa, 2829-516 Caparica, Portugal; di.carreira@campus.fct.unl.pt
[2] CEFITEC, Departamento de Física, Faculdade de Ciências e Tecnologia, Universidade NOVA de Lisboa, 2829-516 Caparica, Portugal; pfr@fct.unl.pt (P.A.R.); mfr@fct.unl.pt (M.R.)
* Correspondence: susana.serio@fct.unl.pt

Abstract: It is currently of huge importance to find alternatives to fossil fuels to produce clean energy and to ensure the energy demands of modern society. In the present work, two types of hybrid solar cell devices were developed and characterized. The photoactive layers of the hybrid heterojunctions comprise poly (allylamine chloride) (PAH) and graphene oxide (GO) and TiO_2 or ZnO films, which were deposited using the layer-by-layer technique and DC-reactive magnetron sputtering, respectively, onto fluorine-doped tin oxide (FTO)-coated glass substrates. Scanning electron microscopy evidenced a homogeneous inorganic layer, the surface morphology of which was dependent on the number of organic bilayers. The electrical characterization pointed out that FTO/$(PAH/GO)_{50}$/TiO_2/Al, FTO/$(PAH/GO)_{30}$/ZnO/Al, and FTO/$(PAH/GO)_{50}$/ZnO/Al architectures were the only ones to exhibit a diode behavior, and the last one experienced a decrease in current in a low-humidity environment. The $(PAH/GO)_{20}$ impedance spectroscopy study further revealed the typical impedance of a parallel RC circuit for a dry environment, whereas in a humid environment, it approached the impedance of a series of three parallel RC circuits, indicating that water and oxygen contribute to other conduction processes. Finally, the achieved devices should be encapsulated to work successfully as solar cells.

Keywords: hybrid solar cells; graphene oxide; zinc oxide; DC-magnetron sputtering; layer-by-layer

Citation: Carreira, D.; Ribeiro, P.A.; Raposo, M.; Sério, S. Engineering of TiO_2 or ZnO—Graphene Oxide Nanoheterojunctions for Hybrid Solar Cells Devices. *Photonics* **2021**, *8*, 75. https://doi.org/10.3390/photonics8030075

Received: 6 February 2021
Accepted: 9 March 2021
Published: 12 March 2021

1. Introduction

The use of renewable energies is of great importance because of the increase in fossil energy costs and to avoid global warming by CO_2 reduction. Solar energy can be considered as sustainable energy, which may effectively satisfy a part of the energy demand of future generations [1,2]. One effective way of converting solar energy into a form like electricity is using solar cells, which are based on the photovoltaic (PV) effect. It has been reported that single-junction crystalline materials such as Si and GaAs can reach power conversion efficiencies (PCEs) up to 30% [3]. Although advances in technology and the mass production of conventional silicon-based solar modules have allowed significant price reductions, this technology presents some limitations, especially regarding material consumption, production speed, and features such as flexibility and form factor. Thus, the development of new solar cell technologies addressing the aforementioned properties is of great importance and interest to the industry.

Twenty years ago, dye-sensitized solar cells (DSSCs) were proposed as low-cost alternatives to the conventional Si solar cells, particularly because of the simplicity of their fabrication processes. DSSCs correspond to the third-generation PV cells category where new trends in the PV technology are applied [4,5]. In first-generation PV cells, an electric interface is created between doped n-type and p-type bulk silicon, and currently, this type of cell offers the highest conversion efficiency [6]. Second-generation PV cells are based on thin-film technology and, as these cells utilize less material, the production

cost significantly drops. Nevertheless, they are less efficient than the bulk cells. Both first- and second-generation cells are based on opaque materials, where front-face illumination and moving supports to follow the sun position are necessary. Third-generation solar cells are based on nanostructured materials and are made of pure organic or a mixture of organic and inorganic components. The nanostructured DSSCs, invented by Michael Grätzel and Brian O'Regan in 1991 [7], is an attractive alternative to the existing solid-state p–n junction solar cells. DSSCs with photoelectric conversion efficiencies of ~12% have been achieved using a liquid electrolyte. Excellent stability data have been obtained for liquid DSSCs, but much less is known about the stability of solid-state DSSCs [8]. A volatile electrolyte will also lead to potential problems on sealing the device, although efficient sealant materials have now been developed. However, fully solid-state DSSCs are less efficient than liquid-type DSSCs, although Kanatzidis's group recently achieved a PCE of 8.5% with a solid-state DSSC [9]. Though considerable progress has been made in improving the PCEs of fully solid-state DSSCs, these cells still suffer from low performance, mainly because of rapid carrier recombination at the various device interfaces [10–12].

Organic conducting polymers with a variety of chemical structures have promising properties, such as easy processing, possible recyclability, relatively low cost, and scalability. Inorganic semiconductors possess better electronic properties, e.g., a high dielectric constant and a high charge mobility and thermal stability [13,14]. To take advantage of both materials, hybrid nanocomposites of inorganic semiconductors and conducting polymers are of great interest, especially as candidates for PV-cell materials, where the combined absorption band of both materials can also better harvest sunlight [15]. Photoinduced charge separation mainly takes place at the interfaces between inorganic semiconductors and conducting polymers in these hybrid materials, where electrons are injected from the conducting polymers into inorganic semiconductors, and holes remain in the polymers. This interfacial charge separation can to some extent prevent the recombination of separated electrons and holes [16]. Several studies have been carried out to find promising combinations of inorganic/organic materials, and optimal hybrid architectures have been attempted; significant progress has been attained in recent years [17,18]. Additionally, one of the materials that has attracted huge interest in the scientific community is graphene and its derivatives (graphene oxide (GO) and reduced graphene oxide (rGO)) [19]. These materials have been extensively studied due to their electrical, mechanical, optical, and thermodynamic properties and are presently used in several applications such as solar cells, solar fuels, lithium-ion batteries, and supercapacitors. In the case of solar cells, these compounds have been used as transparent and nontransparent electrodes, in photoactive layers and in electron transport layers and gaps [20,21].

The morphology of the active layer is another key factor for the device efficiency. In this sense, the n-type and p-type material need to be organized in a morphology that allows high exciton creation and splitting and also good charge carrier transport. Like the organic solar cells, two types of morphologies of active layers are reported in the literature, a planar and a bulk heterojunction [22]. Moreover, surface modifications of the inorganic material are of huge importance, because they can influence the acceptor conduction band, the exciton dissociation efficiency, and thus the open circuit voltage, V_{oc}, and short circuit current, J_{sc}. For example, Goh et al. observed that molecular dipoles and acid–base interactions can lead to TiO_2 band edge shift, inducing a change in V_{oc} for hybrid solar cells with poly(3-hexylthiophene-2,5-diyl) (P3HT) [23]. Analogously, the conjugated polymers can be modified, as demonstrated by Krüger et al., where the functionalization of both chain ends of P3HT with cyanoacetic groups improved the charge injection efficiency and the power conversion efficiency [24].

Notwithstanding, choosing material arrangements with appropriate properties and matching work functions, loss mechanisms need to be addressed and minimized in order to achieve solar cells devices with high power conversion efficiencies. All the factors mentioned above represent an important challenge and must be considered in the development of hybrid solar cells.

Thus, and within the frame of work carried out in the last years under organic conductive polymers, photoluminescent and photochromic [25–27], and also on semiconductors oxides films, such as TiO_2 and ZnO [28,29], the present work was undertaken in order to contribute solutions to capture and convert solar energy. For that, two types of hybrid solar cell devices were developed and studied: FTO/$(PAH/GO)_x$/TiO_2/Al and FTO/$(PAH/GO)_x$/ZnO/Al, where x is the number of bilayers. The achieved results reported herein point out that the obtained devices present properties and characteristics that can be successfully applied to solar cells.

2. Materials and Methods

All chemicals used in this work were of analytical grade or chemical grade (Sigma-Aldrich).

2.1. Materials

In this work, two types of solid supports were used depending on the type of electrical characterization to be performed, namely fluorine-doped tin oxide (FTO)-coated glass substrates (TEC15, 12−14 Ω/□) purchased from Solaronix (Aubonne, Switzerland, dimensions 39 mm × 15 mm) and glass substrates with deposited interdigitated electrodes (IDE) purchased from DropSens (Oviedo, Asturias, Spain). The IDE glass substrates were formed by BK7 glass with deposited gold interdigitated electrodes (G-IDEAU10) with dimensions 22.8 × 7.6 × 0.7 mm, and each 'finger' was 10 µm in width, which had the same spacing between them.

The used gases argon, oxygen, and nitrogen had a ≥99.9% purity.

2.2. Devices Preparation

The development of devices involved three phases, described below, in order to obtain the desired architecture (see Figure 1a). Figure 1b depicts a schematic illustration of the energy band diagram of the developed devices [30].

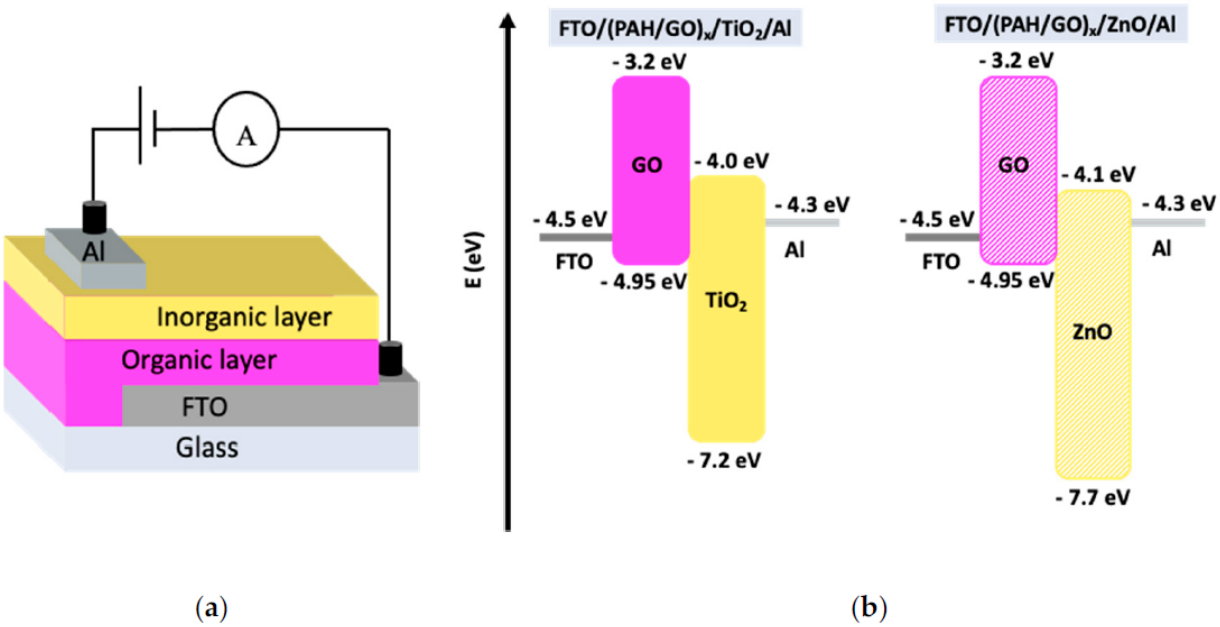

Figure 1. (**a**) Representative scheme of the developed hybrid solar cell architectures. (**b**) Schematic representation of the energy band diagram of the developed devices.

2.2.1. Organic Layer Deposition

Thin films of the polyelectrolyte poly (allylamine hydrochloride) (PAH) (average Mw = 50,000–65,000 g/mol) and graphene oxide GO (CAS number 777676), both purchased from Sigma-Aldrich (Steinheim, Germany), were prepared by the layer-by-layer

technique [25,27]. This technique consists of the alternating adsorption of cationic and anionic polyelectrolytes on solid substrates.

For the present work, aqueous solutions of the PAH polyelectrolyte were prepared with a concentration of 10^{-2} M by dissolving 0.0234 g of PAH granules in 25 mL of ultra-pure water (Milli-Q, with a resistivity of 18.2 MΩ cm at 25 °C). This water was used in all solutions and also as washing solution. The GO solutions were obtained by dissolving 0.5 mL of GO aqueous solution with a concentration of 4 mg/mL in 24.5 mL of ultra-pure water to obtain a concentration of 0.5×10^{-2} M.

In the preparation of PAH/GO LbL films, the solid supports (FTO-coated glass substrates or IDE glass substrates) were first immersed in the PAH aqueous solution during a period of 1 min, thereby adsorbing a positively charged polyelectrolyte layer. After this adsorption, the substrate was washed with ultra-pure water (washing solution) to remove excess molecules or aggregates that have not been completely adsorbed. Subsequently, the substrate was also immersed in the anionic GO aqueous solution for 1 min. The adsorption times were chosen, considering studies of adsorption kinetics carried out by the group. After adsorption of the anionic layer, the substrate was again washed with ultra-pure water to remove the nonadsorbed molecules and was then dried with a stream of nitrogen (99.9% purity, Air Liquide).

To note, drying with nitrogen was decisive in obtaining the desired films, as studies performed without drying with nitrogen at the end of each bilayer showed that after a few bilayers (~5), the film began to desorb and the solution of GO precipitated. Therefore, the drying nitrogen step was introduced in the layer-by-layer technique.

After the aforementioned sequence, a film with a bilayer was obtained. The procedure described above was repeated according to the number of bilayers, x, that was intended in the film, with the LbL film designated by $(PAH/GO)_x$. In this work, devices with 20, 30, and 50 bilayers of PAH/GO were prepared using the procedure described above.

Before the deposition of the LbL films, the FTO and IDE glass substrates were washed with isopropanol, acetone, and ultra-pure water in this order, and then dried with a stream of nitrogen just before use. This procedure, besides guaranteeing the cleaning of the substrates, also allow them to be negatively charged, thus allowing adsorption of the PAH (positive charge) layer. In addition, to prevent contact between the electrodes of the devices in the case of the FTO glass substrates, a portion of the FTO film—approximately 10 mm × 15 mm —was removed on all substrates using a solution of zinc (Zn) with hydrochloric acid (HCl). The solution was applied to the desired area during a period of about 24 h.

2.2.2. Inorganic Layer Deposition

The next phase consisted of the deposition of the inorganic layer (TiO_2 or ZnO), for the FTO glass substrates with an organic layer, which was carried out by DC-reactive magnetron sputtering.

Titanium and zinc discs (Goodfellow, Huntingdon, England, 99.99% purity) of 64.5 mm in diameter and 4 mm in thickness each were used as the sputtering targets. A turbomolecular pump (Pfeiffer TMH 1001, Pfeiffer Vacuum GmbH, Asslar, Germany) was used to attain a base pressure of $10^{-4}-10^{-5}$ Pa (before introducing the sputtering gas). Before the sputter-deposition step of the films, a movable shutter was interposed between the target and the substrates. The target was pre-sputtered in Ar atmosphere for 2 min to clean the target surface. The target-to-substrate distance was kept constant at 100 mm. Gases in the system were pure Ar and O_2 (both 99.99%, Air liquide) and their pressures were separately controlled by needle valves.

TiO_2 and ZnO depositions were both carried out in 100% O_2 atmosphere. For the TiO_2 film, the total pressure was kept constant at 2 Pa, the sputtering power was 530 W, and the deposition time was 25 min. In the case of the ZnO film, the total pressure was fixed at 4.8 Pa, the sputtering power was 300 W, and the deposition time was 30 min. The target-to-substrate distance was kept constant at 100 mm. No external substrate heating was

used during the depositions. The substrate temperature was measured by a thermocouple passing through a small hole in a copper piece, which was placed in contact with the substrate. During the deposition process, the sample temperature increased up to 60 °C due to the bombardment of plasma particles of the substrate.

2.2.3. Aluminum Electrode Deposition

Finally, to obtain the desired solar cell architecture (see Figure 1), an aluminum electrode was deposited by thermal evaporation over an area of approximately 0.95 cm^2. The Al electrodes' deposition was carried out with Al wires of high purity (Advent Research Materials, Oxford, England, 99.5%) placed on a spiral tungsten resistor in a vacuum chamber, and the films were mounted on a vertical support at about 10 cm from the tungsten resistor. The deposition was performed with a pressure of $10^{-5}-10^{-6}$ mbar assured by a turbomolecular pump, an applied current of 50 A, and a deposition time of 1 min.

2.3. Characterization Techniques

The characterization of the thin film's morphology was carried out by a field emission scanning electron microscope (FEG-SEM JEOL 7001F) operating at 15 keV. A chromium thin film was coated on the films surface before SEM analysis to prevent charge build-up. The device's architecture was evaluated from the SEM cross-sectional images.

The electric measurements (I–V characteristic curve) of the final devices were carried out using a programmable DC power supply model Rigol DP811A (programmable DC power supply, LX1, Telonic Instruments, Berkshire, UK) in the absence of light, at ambient light, and with light from a 250 W halogen lamp positioned at 40 cm from the device. All the I–V measurements were performed by changing the voltage between 0 and ~1.5 V, with an increment of 50 mV at room temperature, which was guaranteed by a vent placed in the measurement system.

The electrical analysis of $(PAH/GO)_{20}$ onto BK7 solid support with gold interdigitate electrodes was carried out by measuring the impedance spectra of this device in air or in argon atmosphere, both at ambient light with a Solartron 1260 Impedance Analyzer (Solartron Analytical, AMETEK scientific instruments, Berwyn, PA, USA) in the frequency range of 1 Hz–1 MHz, applying an AC voltage of 25 mV. All measurements were performed at room temperature 25 °C.

All devices were stored in the dark inside a desiccator with silica gel to control the humidity.

3. Results and Discussion

3.1. Build-Up of PAH and GO LbL Films

PAH and GO LbL films were prepared with different numbers of layers, namely, 20, 30, and 50 bilayers. The growth of these films was previously characterized by measuring the UV-vis absorbance spectra as a function of the number of bilayers, and a linear film growth was detected, as is reported in detail elsewhere [31]. Although the aforementioned linearity is easily perceived, it should be noted that in the classic LbL technique, a linear film growth is not commonly detected in the adsorption of the first bilayers. This phenomenon can be explained by the roughness of the used substrate and uneven distribution of charges over the surface substrate [32].

3.2. Morphological Characterization

The developed devices were characterized by scanning electron microscopy to study the morphology and to evaluate if the desired architecture was obtained. By the SEM cross-sectional images analysis, images not shown, it was verified that all the developed devices exhibited the desired architecture. On the other hand, the surface SEM images reveal for all samples a uniform surface with no apparent defects, such as the presence of cracks, which could limit or prevent the normal functioning of devices.

For the TiO_2-based devices (Figure 2), the formation of aggregates of grains can be noticed, ranging from 260 to 400 nm for the devices with 20 bilayers and from 200 to 340 nm for the devices with 30 bilayers. In the case of the device with 50 bilayers, much smaller aggregates were detected (of the order of 20–30 nm). Moreover, the SEM images reveal that TiO_2 films follow the underlying rough FTO morphology, although they present a more granular morphology due to the organic layer deposited just below. The surface of the aluminum electrodes was also analyzed and, as can be observed in Figure 2, the surface was also homogeneous with no signs of cracks. The morphology was like the one detected for the TiO_2 films, with changes also being observed with the number of bilayers of the organic film.

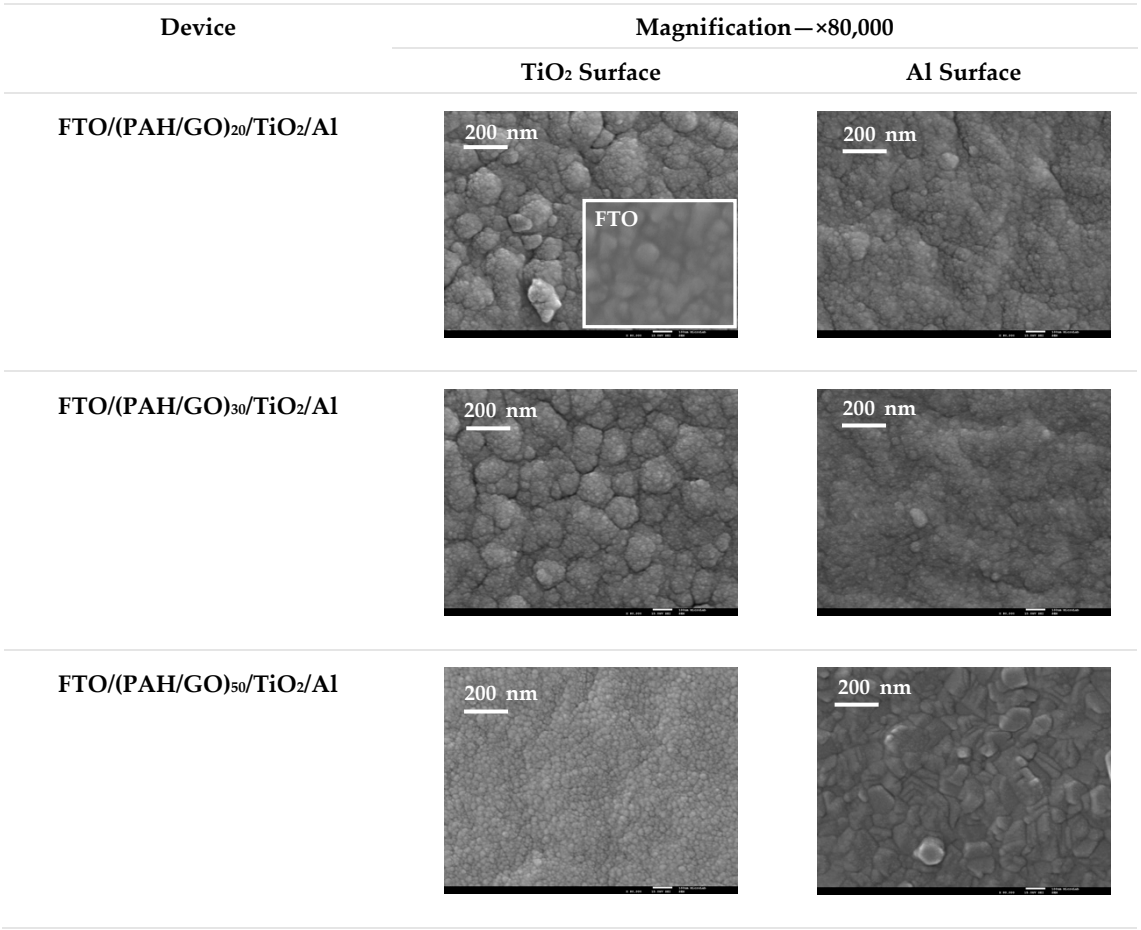

Figure 2. SEM images for devices with the architecture $(FTO/PEI/GO/TiO_2/Al)_x$, with x = 20, 30, and 50 bilayers. Inset depicts the FTO SEM image taken with the same magnification.

In the case of the devices with ZnO as the inorganic layer, for all samples, a homogeneous surface is observed with no sign of cracks (Figure 3) for the aluminum electrode. In addition, for these devices, the SEM images evidenced the presence of aggregates, which do not present significant differences in their dimensions between the analyzed devices, being independent of the number of the organic bilayers. Their dimensions ranged between approximately 50 and 200 nm and, in comparison, these values are considerably lower than those observed for the TiO_2 films. The surface morphology of the Al electrode was also like the one detected for the corresponding ZnO film, as can be observed in Figure 3.

Device	Magnification ×80,000	
	ZnO Surface	Al Surface
FTO/(PAH/GO)$_{20}$/ZnO/Al	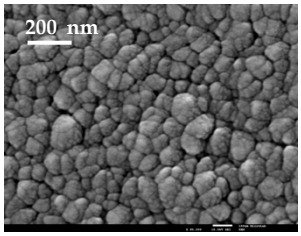	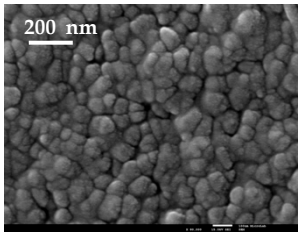
FTO/(PAH/GO)$_{30}$/ZnO/Al	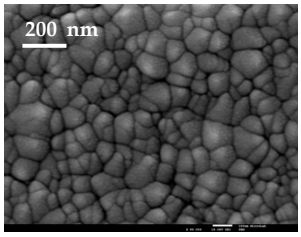	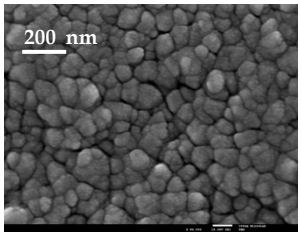
FTO/(PAH/GO)$_{50}$/ZnO/Al	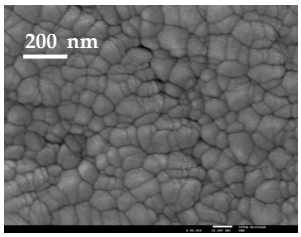	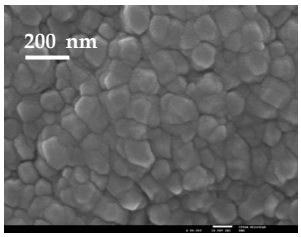

Figure 3. SEM images for three devices with the architecture (FTO/PEI/GO/ZnO/Al)$_x$, with x = 20, 30, and 50 bilayers.

It should be noted that the surface morphology is completely different for the TiO_2 and ZnO devices. For TiO_2 films, the agglomerates of grains are distributed over the substrate surface with a 'blooming flower-like' appearance. In the case of ZnO films, the surface presents a pronounced cone-like morphology.

The results of the morphological characterization performed for both inorganic films (TiO_2 and ZnO) are in good agreement with the ones reported recently elsewhere, which were produced in similar conditions [33].

3.3. Influence of the Number of Bilayers on the Electric Properties of FTO/(PAH/GO)$_x$/TiO_2/Al and FTO/(PAH/GO)$_x$/ZnO/Al (x = 20 and 30)

To analyze the influence of the surrounding environment on the electrical properties of the devices, samples with 20 and 30 PAH/GO bilayers were analyzed at room temperature, at a temperature ranging from 20 °C to 25 °C, with a relative humidity (RH) between 50% and 60%, for both types of devices.

In the case of TiO_2 devices, the characterization was performed only in ambient light, in an environment without light interaction, and is reported in detail in [31]. For both devices, a linear dependence of the current with the applied voltage was observed, and thus, a resistive behavior, which was not expected. This can be attributed to the high resistance at the photoactive electrode layer interface, thus blocking a large portion of the charge carriers and/or the existence of an inefficient donor–acceptor junction, which will lead to an inefficient transport of charges to the electrodes. Based on these results, both devices were not analyzed when exposed to a light spot.

On the other hand, for ZnO-based devices, the results evidenced for the device with 20 bilayers a typical resistive behavior, where the current depends linearly on the applied

voltage to the device terminals [31]. For all the measurements performed, no significant hysteresis effect was observed, and no change in its electrical behavior was detected when exposed to ambient light. In turn, the sample with 30 PAH/GO bilayers exhibited a behavior very close to what would be expected for a diode. In comparison with the other devices, the behavior of this device seemed to change when exposed to the light spot from a halogen lamp. Nevertheless, based on the analysis of its current–voltage characteristic curve, it was concluded that the slight increase in current in the presence of light was not significant enough to be considered a photosensitivity phenomenon.

3.4. Comparison of the Electric Properties of FTO/(PAH/GO)$_{50}$/TiO$_2$/Al and FTO/(PAH/GO)$_{50}$ /ZnO/Al

To understand why the previously presented devices exhibited a poor performance, a device with 50 bilayers was produced. The increase in the number of bilayers is expected to prevent the aluminum migration inside the device, which occurred in previous works carried out by the group [34], although the SEM characterization did not reveal such an effect. Moreover, this device was analyzed inside a desiccator, where the temperature ranged from 20 °C to 23 °C, with a very low relative humidity, varying from 10% and 15%, because these parameters can also influence the characterization of the sample. The obtained current–voltage curves are depicted in Figure 4 for both types of devices. Though this experimental setup enabled a more accurate control of temperature and humidity, it did not allow the characterization of the device under the action of a light spot.

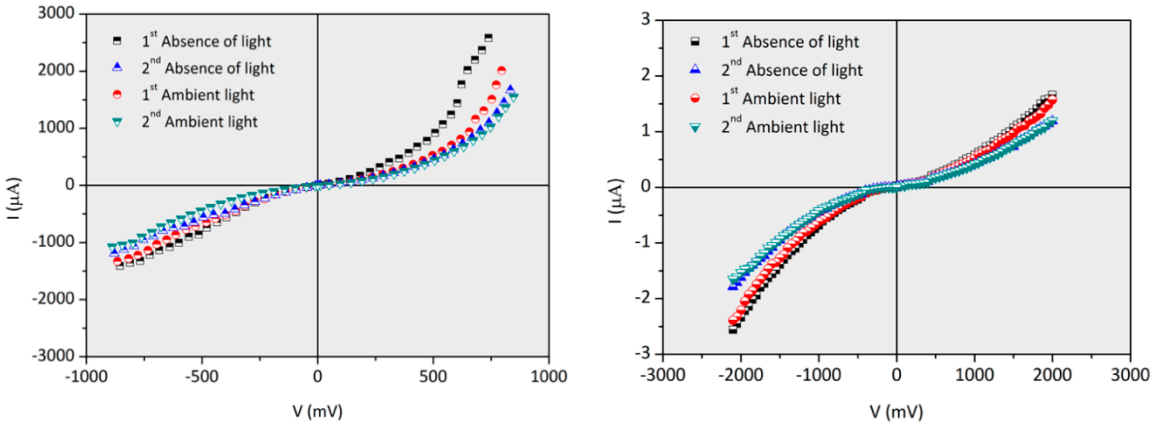

(**a**) (**b**)

Figure 4. Comparison of the electrical properties of (**a**) (FTO/PAH/GO/TiO$_2$/Al)$_{50}$ and (**b**) (FTO/PAH/GO/ZnO/Al)$_{50}$ for different light conditions, in a low-relative-humidity environment. Adapted from [27].

For the TiO$_2$ device, the analysis of the results evidenced a characteristic curve of a diode and hysteresis effect. This phenomenon is particularly evident from the first to the second measurement for both illumination conditions, which suggests that the degradation of the organic films most likely occurred, leading to a less conductive device. It should be noted that this device was more conductive when positively polarized (see Figure 4).

For the ZnO device, a similar behavior is observed to the one expected for a diode-type device.

The analysis of Figure 4 further revealed that between the first and second measurements and between the third and fourth, the hysteresis effect is reduced, with no significant current decrease between them. Still, this effect is particularly evident between the second and third measurements. Again, for this device, no current increase was observed in the presence of light, and therefore, it is not photosensitive. Considering the quotient between the applied voltage values and the obtained current values, this device was much less conductive than the others. It is important to note that this device was analyzed in an environment with 10% relative humidity, and this parameter can be a key factor on the

conduction of the developed solar cells. In fact, according to the literature [35], the presence of moisture and/or oxygen plays a major role in the conduction of organic films, making them more conductive.

3.5. Electric Characterization of $(PAH/GO)_{20}$ onto IDE Gold Electrodes Glass Substrates

3.5.1. $(PAH/GO)_{20}$ onto IDE Gold Electrodes Glass Substrates: I–V Curves

To understand the influence of the environmental conditions on the performance of the organic layer and, consequently, on the produced hybrid solar cells, devices with 20 bilayers of PAH/GO were developed. The choice of this number of bilayers was based on preliminary studies carried out by the group that showed that this number leads to an adequate thickness in order to avoid short circuit of the devices, besides requiring less material and lower production time compared with the other developed devices. The study of this organic solar cell involved several phases, addressing different environmental conditions.

In this sense, the first measurements were carried out in ambient light, with a relative humidity of approximately 55% and at a temperature of 21 °C. As can be seen from Figure 5a, in these conditions, the device has a purely ohmic conduction mechanism. It should be noted that the hysteresis effect is quite noticeable, with an increase in the conductivity of the sample being detected, from the first to the second measurement. After a period of about 24 h, new measurements were performed sequentially, with the first measurement carried out under similar conditions than the ones mentioned before. On the other hand, the following measurements were carried out in a beaker with argon atmosphere, and the results are depicted in Figure 5b. The obtained results corroborate what was expected: The absence of moisture and oxygen leads to the less conductive devices. It is also easily observed that the slope of the fourth and fifth measurements is considerably lower than the one observed in the third measurement, which is indicative of an increase in its resistivity.

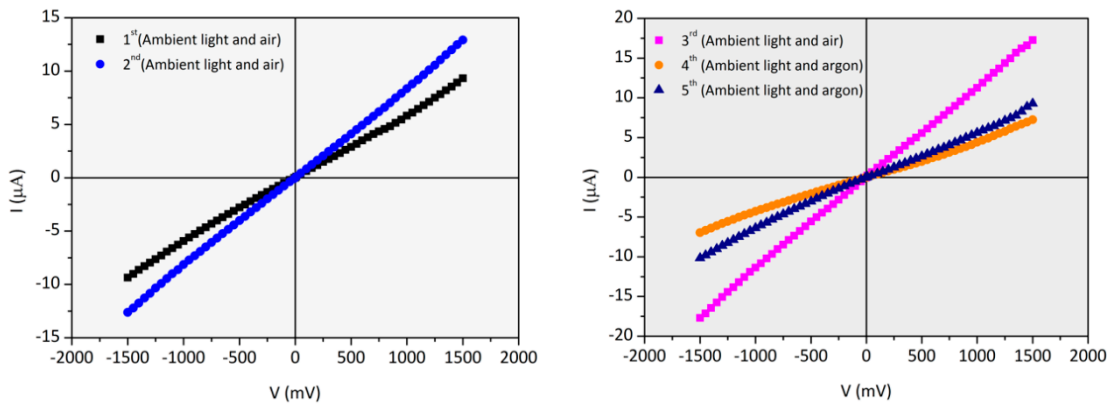

(**a**) (**b**)

Figure 5. (**a**) Current–voltage curves of a $(PAH/GO)_{20}$ film in air, in the presence of ambient light. (**b**) Current–voltage curves of a $(PAH/GO)_{20}$ film in air, in the presence of ambient light and in a beaker with argon.

To understand whether these changes in conductivity were reversible, two new measurements (sixth and seventh) were performed, in an environment with humidity and in ambient light. The corresponding current–voltage curves are shown in Figure 6a, where it is possible to observe a significant change in the behavior of the device. Between these consecutive measurements, the behavior of the device appears to approach a diode instead of the already observed ohmic behavior.

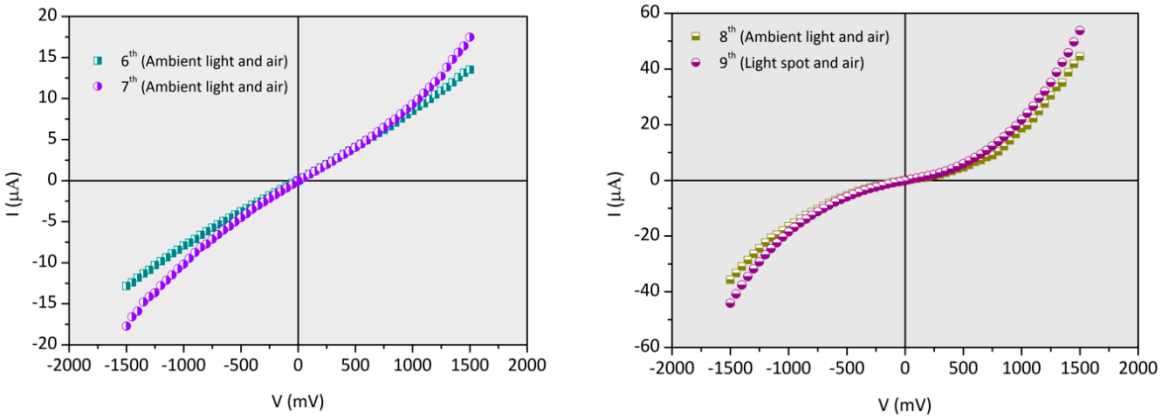

(**a**) (**b**)

Figure 6. (**a**) Current–voltage curves of a $(PAH/GO)_{20}$ film in air, in the presence of ambient light. (**b**) Current–voltage curves of a $(PAH/GO)_{20}$ film in air, in the presence of ambient light and a light spot.

In addition, it was also possible to conclude that changes in the conductivity of these films (due to the presence or absence of moisture and/or oxygen) have a high rate of reversibility, as current values were recorded close to the initial ones, indicating that there are no chemical reactions that can degrade organic compounds, under the tested experimental conditions.

To finalize the characterization of this device, its photosensitivity was evaluated by performing two measurements (eighth and ninth) with a relative humidity of about 55%. The first measurement of this study was performed when the sample was exposed to ambient light, while the second was exposed to a light spot from a halogen lamp. The obtained curves are shown in Figure 6b and the results evidence that this device has acquired a diode behavior, after being subjected to successive applied electric fields. This behavior change may be related to the reduction of the graphene oxide due to the applied electric fields [36]. Moreover, the reduction process causes a decrease in the resistance of the sheet of graphene oxide (R_s), making it easier to transport charges [19]. An increase in the current produced by the cell is also noticeable, when it is exposed to the light spot, which suggests that this device with the 20 PAH/GO bilayers has photosensitivity, unlike those in which the inorganic layer was deposited.

3.5.2. $(PAH/GO)_{20}$ onto IDE Gold Electrodes Glass Substrates: Impedance Spectra

The analysis of $(PAH/GO)_{20}$ by impedance spectroscopy involved different sets of measurements, performed in two different environments.

- Dry environment

These measurements were carried out in ambient light, inside a beaker with argon, with the intention of reducing the presence of oxygen and/or humidity, elements that could influence the sample behavior. The corresponding Nyquist diagram is presented in Figure 7a. The observation of the diagram allows the inference that it corresponds to a semicircle, in which neither the real nor imaginary component deviate from the origin. It is also observed that there is an inverse behavior between the resistive and reactive part of the impedance: For low frequencies, there is a decrease in the reactive component and an increase in the resistive component, while for high frequencies, the opposite occurs. Figure 7 also presents the graph of the resistive component of the device's impedance (Z') as a function of the angular frequency (ω), which shows that up to 10^4 rad·s^{-1}, the Z' value

remains constant and decreases for higher frequencies (Figure 7a). The fitting performed to the obtained data was based on the following equation:

$$Z' = \frac{A}{1 + (B \times \omega)^2} \quad (1)$$

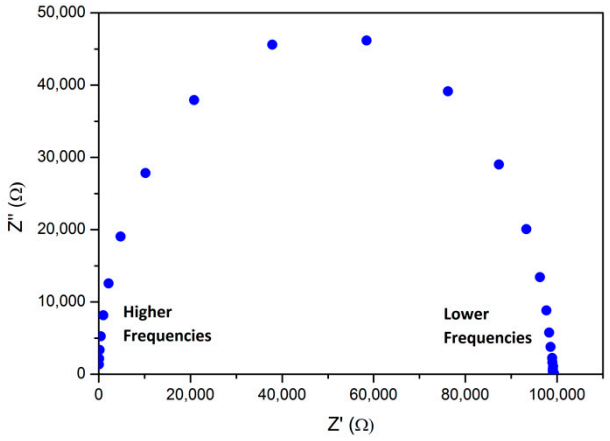

(**a**)

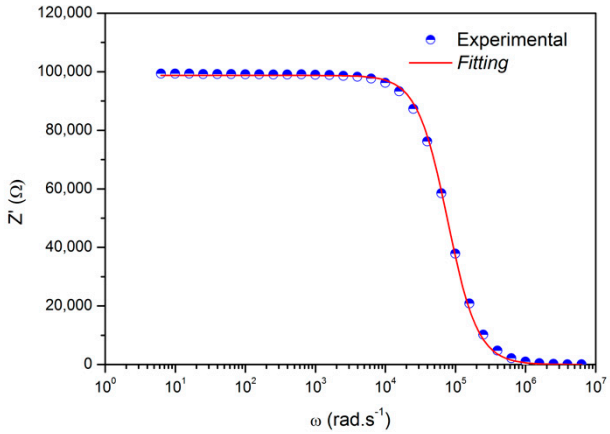

(**b**)

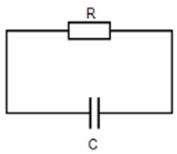

(**c**)

Figure 7. (**a**) Nyquist diagram obtained by impedance spectroscopy for a $(PAH/GO)_{20}$ film deposited on a substrate with gold interdigitated electrodes in an argon atmosphere. (**b**) Real impedance component as a function of angular frequency. In red, the adjustment made to the experimental points is shown. (**c**) Equivalent circuit of a PAH/GO film with 20 bilayers analyzed by impedance spectroscopy. R and C are the resistor and capacitor, respectively.

This equation corresponds to the real impedance part of an RC circuit in parallel (see Figure 7c), where the A parameter corresponds to the resistance (R) value, and the B parameter corresponds to the product of resistance by capacitance (RC) at the angular

frequency ω. The best adjustment to the experimental points was achieved with the A and B parameters of Equation (1), taking the values presented in Table 1.

Table 1. Estimated parameter (A, B, C, D, E, and/or F) values through the fitting with Equation (1) or (2) to the real part values of the measured impedance in different environmental conditions.

Environmental Conditions	Equation	A (R1[Ω])	B (R1C1[s])	C (R2[Ω])	D (R2C2[s])	E (R3[Ω])	F (R3C3[s])
Dry (<10% RH)	(1)	98 747	1.3×10^{-5}	—	—	—	—
Humid (50–60% RH)	(2)	30,060	0.05457	11,642	6.2×10^{-4}	17,513	3.5×10^{-6}

- Humid environment

The second set of measurements was also carried out under ambient light, but in air, with a relative humidity between 50% and 60%. The Nyquist diagram shown in Figure 8a differs from that shown in Figure 7a, in which the system impedance was equivalent to an RC circuit in parallel.

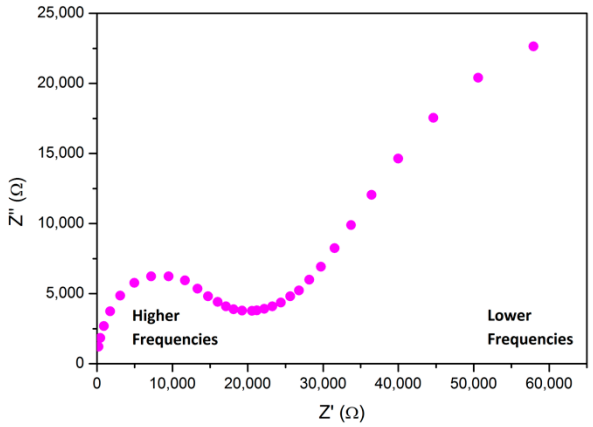

(**a**)

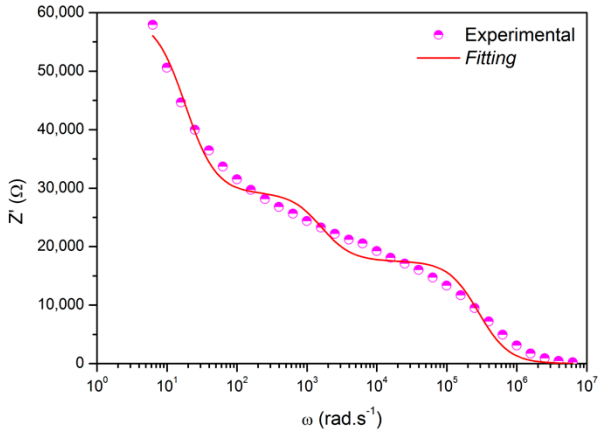

(**b**)

Figure 8. *Cont.*

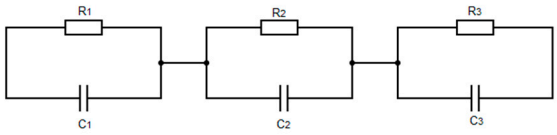

(**c**)

Figure 8. (**a**) Nyquist diagram obtained by impedance spectroscopy for a $(PAH/GO)_{20}$ film deposited on a substrate with gold interdigitated electrodes in air. (**b**) Real impedance component as a function of angular frequency. In red, the adjustment made to the experimental points is shown. (**c**) Equivalent circuit of a PAH/GO film with 20 bilayers analyzed by impedance spectroscopy. R and C are the resistor and capacitor, respectively.

Thus, given the differences between the two diagrams, it is possible that, in the case where the sample was analyzed in the air, several conduction mechanisms contribute to the presented behavior, in addition to the resistive and reactive part of a single RC circuit. Figure 8b shows that the behavior of the resistive part of the impedance is not typical of a single RC circuit. In this sense, the curve that best fitted the experimental points was obtained using the following equation:

$$Z' = \frac{A}{1 + (B \times \omega)^2} + \frac{C}{1 + (D \times \omega)^2} + \frac{E}{1 + (F \times \omega)^2} \quad (2)$$

The equation presented above then reflects the actual impedance component of three RC circuits in parallel, as shown in Figure 8c. Thus, A corresponds to R_1, B to R_1C_1, C to R_2, D to R_2C_2, E to R_3, and F to R_3C_3. Again, the parameter ω represents the angular frequency of the system. The obtained results are summarized in Table 1.

Although this model of three parallel RC circuits in series does not fully fit the experimental data, the obtained result suggests that, in addition to the behavior of polymer molecules and graphene oxide, there are at least two other constituents, oxygen and water vapor, that decrease the impedance of the film, which is in accordance with the other obtained data for the devices with the inorganic layer. This means that these devices must be encapsulated to work properly as solar cells.

4. Conclusions

In this work, two types of solar cell devices: FTO/$(PAH/GO)_x$/TiO_2/Al and FTO/$(PAH/GO)_x$/ZnO/Al (x—number of bilayers), were developed.

The morphological characterization evidenced larger aggregates for the TiO_2-based devices in comparison with ZnO devices with 20 and 30 PAH/GO bilayers, where the surface morphology is dependent on the number of bilayers, while for ZnO devices, no change in the aggregates size was detected with the number of bilayers.

Based on the electrical characterization, a resistive behavior was detected for TiO_2-based devices with 20 and 30 PAH/GO bilayers, without photosensitivity when analyzed in air at ambient light, which may be due to the high resistance between the photoactive layer and the electrode or to an inefficient donor–acceptor interface. Regarding the TiO_2 device with 50 bilayers of PAH/GO, analyzed inside a desiccator to reduce moisture, a characteristic I–V curve of a diode was observed, which was more conductive when positively polarized. In the case of the ZnO-based devices with 20 bilayers of PAH/GO, an ohmic behavior was detected, and with 30 bilayers, a semiconductor behavior was revealed. A slight increase in current was recorded with the latter sample when exposed to a light spot from a halogen lamp. In the device with 50 bilayers, a typical diode behavior was detected, although it was much less conductive than all the other samples analyzed. In fact, it was studied inside a desiccator, with a relative humidity close to 10%, which allowed the conclusion that humidity is a key factor in the conduction of the organic films.

The study of the organic layer performed with the $(PAH/GO)_{20}$ device initially revealed a typical resistance behavior; however, during the measurements, a diode behavior was acquired. When placed in an Ar atmosphere, the sample proved to be less conductive. The device was also subjected to a light spot, where an increase in current was observed, demonstrating its photosensitivity. Regarding the impedance spectroscopy analysis under ambient light and in Ar atmosphere, the Nyquist diagram showed an increase in the resistive component of the impedance of the sample (real component) for low frequencies, while for high frequencies, it decreased. The reactive component (imaginary component) presented an inverse behavior, thus suggesting that the sample's equivalent circuit in these conditions is an RC circuit in parallel. In the study of this device under ambient light but performed at air, the Nyquist diagram evidenced a behavior dependent on the contribution of several conduction mechanisms. Therefore, it was possible to conclude that the equivalent circuit of the sample consisted of three parallel RC circuits in series, meaning that these devices should be encapsulated to work properly. This work further evidences that the use of ZnO as an electron acceptor material in a solar cell appears to be more suitable for the performance of such devices than TiO_2, and the conduction mechanisms of the devices are influenced by the surrounding environment and surface morphology of the inorganic layer.

Author Contributions: Conceptualization, D.C., M.R. and S.S.; methodology, D.C., M.R. and S.S.; software, D.C.; validation, D.C., P.A.R., M.R. and S.S.; formal analysis, D.C., P.A.R., M.R. and S.S.; investigation, D.C.; resources, P.A.R., M.R. and S.S.; data curation, D.C.; writing—original draft preparation, S.S.; writing—review and editing, D.C., P.A.R., M.R. and S.S.; visualization, D.C., P.A.R., M.R. and S.S.; supervision, M.R. and S.S.; project administration, S.S.; funding acquisition, P.A.R., M.R. and S.S. All authors have read and agreed to the published version of the manuscript.

Funding: This work was supported by the Centre of Physics and Technological Research CEFITEC, which is financed by national funds from FCT/MEC (UID/FIS/00068/2019). The authors also acknowledge and appreciate the support given to CEFITEC by the Portuguese Foundation for Science and Technology (FCT) through the strategic project UID/FIS/00068/2020.

Institutional Review Board Statement: Not applicable.

Informed Consent Statement: Not applicable.

Data Availability Statement: Not applicable.

Acknowledgments: The authors acknowledge the financial support from FEDER, through Programa Operacional Factores de Competitividade—COMPETE and Fundação para a Ciência e a Tecnologia—FCT, for the project UID/FIS/00068/2020.

Conflicts of Interest: The authors declare no conflict of interest.

References

1. International Energy Outlook. 2020. Available online: http://www.eia.doe.gov/oiaf/ieo/index.html (accessed on 1 February 2021).
2. The Intergovernmental Panel on Climate Change. Climate Change and Land. 2019. Available online: http://www.ipcc.ch (accessed on 1 February 2021).
3. Green, M.A.; Hishikawa, Y.; Dunlop, E.D.; Levi, D.H.; Hohl-Ebinger, J.; Yoshita, M.; Ho-Baillie, A.W.Y. Solar cell efficiency tables (Version 53). *Prog. Photovolt. Res. Appl.* **2019**, *23*, 3–12. [CrossRef]
4. Alaaeddin, M.H.; Sapuan, S.M.; Zuhri, M.Y.M.; Zainudin, E.S.; L-Oqla, F.M.A. Photovoltaic applications: Status and manufacturing prospects. *Renew. Sustain. Energy Rev.* **2019**, *102*, 318–332. [CrossRef]
5. Brown, G.F.; Wu, J. Third generation photovoltaics. *Laser Photonics Rev.* **2009**, *3*, 394–405. [CrossRef]
6. Shockley, W.; Queisser, H.J. Detailed Balance Limit of Efficiency of p-n Junction Solar Cells. *J. Appl. Phys.* **1961**, *32*, 510. [CrossRef]
7. O'Regan, B.; Gratzel, M. A low-cost, high-efficiency solar-cell based on dye- sensitized colloidal TiO_2 films. *Nature* **1991**, *353*, 737–740. [CrossRef]
8. Wu, J.; Lan, Z.; Hao, S.; Li, P.; Lin, J.; Huang, M.; Fang, L.; Huang, Y. Progress on the electrolytes for dye-sensitized solar cells. *Pure Appl. Chem.* **2008**, *80*, 2241–2258. [CrossRef]

9. Chung, I.; Lee, B.; He, J.; Chang, R.P.; Kanatzidis, M.G. All-solid-state dye-sensitized solar cells with high efficiency. *Nature* **2012**, *485*, 486–489. [CrossRef]
10. Hyuk, I.S.; Sun, L.C.; Ah, C.J.; Hui, L.Y.; Nilkamal, M.; Jung, K.H.; Nazeeruddin, M.K.; Michael, G.; Il, S.S. Toward interaction of sensitizer and functional moieties in hole-transporting materials for efficient semiconductor-sensitized solar cells. *Nano Lett.* **2011**, *11*, 4789–4793.
11. Chang, J.A.; Im, S.H.; Lee, Y.H.; Kim, H.J.; Lim, C.S.; Heo, J.H.; Seok, S.I. Panchromatic photon-harvesting by hole-conducting materials in inorganic–organic heterojunction sensitized-solar cell through the formation of nanostructured electron channels. *Nano Lett.* **2012**, *12*, 1863–1867. [CrossRef]
12. Im, S.H.; Kim, H.-J.; Kim, S.W.; Kim, S.-W.; Seok, S.I. All solid state multiply layered PbS colloidal quantum-dot-sensitized photovoltaic cells. *Energy Environ. Sci.* **2011**, *4*, 4181–4186. [CrossRef]
13. Hou, W.; Xiao, Y.; Han, G.; Lin, J.-Y. The Applications of Polymers in Solar Cells: A Review. *Polymers* **2019**, *11*, 143. [CrossRef]
14. Luceño-Sánchez, J.A.; Díez-Pascual, A.M.; Capilla, R.P. Materials for photovoltaics: State of art and recent developments. *Int. J. Mol. Sci.* **2019**, *20*, 976. [CrossRef] [PubMed]
15. Wright, M.; Uddin, A. Organic-inorganic hybrid solar cells: A comparative review. *Sol. Energy Mater. Sol. Cells* **2012**, *107*, 87–111. [CrossRef]
16. Narayan, M.; Singh, J. A theoretical study on the operation principle of hybrid solar cells. *Electronics* **2015**, *4*, 303–310. [CrossRef]
17. Fan, X.; Zhang, M.; Wang, X.; Yang, F.; Meng, X. Recent progress in organic-inorganic hybrid solar cells. *J. Mater. Chem. A* **2013**, *1*, 8694–8709. [CrossRef]
18. Roland, S.; Neubert, S.; Albrecht, S.; Stannowski, B.; Seger, M.; Facchetti, A.; Schlatmann, R.; Rech, B.; Neher, D. Hybrid Organic/Inorganic Thin-Film Multijunction Solar Cells Exceeding 11% Power Conversion Efficiency. *Adv. Mater.* **2015**, *27*, 1262–1267. [CrossRef]
19. Chen, D.; Feng, H.; Li, J. Graphene oxide: Preparation, functionalization, and electrochemical applications. *Chem. Rev.* **2012**, *112*, 6027–6053. [CrossRef] [PubMed]
20. Yang, Y.; Han, C.; Jiang, B.; Iocozzia, J.; He, C.; Shi, D.; Jiang, T.; Lin, Z. Graphene-based materials with tailored nanostructures for energy conversion and storage. *Mater. Sci. Eng. R Rep.* **2016**, *102*, 1–72. [CrossRef]
21. Hu, C.; Song, L.; Zhang, Z.; Chen, N.; Feng, Z.; Qu, L. Tailored graphene systems for unconventional applications in energy conversion and storage devices. *Energy Environ. Sci.* **2015**, *8*, 31–54. [CrossRef]
22. Zhao, L.; Lin, Z. Crafting Semiconductor Organic—Inorganic Nanocomposites via Placing Conjugated Polymers in Intimate Contact with Nanocrystals for Hybrid Solar Cells. *Adv. Mater.* **2012**, *24*, 4353–4368. [CrossRef] [PubMed]
23. Goh, C.S.; Scully, R.; McGehee, M.D. Effects of molecular interface modification in hybrid organic-inorganic photovoltaic cells. *J. Appl. Phys.* **2007**, *101*, 114503. [CrossRef]
24. Kruger, R.A.; Gordon, T.J.; Baumgartner, T.; Sutherland, T.C. End-Group Functionalization of Poly(3-hexylthiophene) as an Efficient Route to Photosensitize Nanocrystalline TiO_2 Films for Photovoltaic Applications. *ACS Appl. Mater. Interfaces* **2011**, *3*, 2031–2041. [CrossRef] [PubMed]
25. Ferreira, Q.; Gomes, P.J.; Ribeiro, P.A.; Jones, N.C.; Hoffmann, S.V.; Mason, N.J.; Oliveira, O.N., Jr.; Raposo, M. Determination of Degree of Ionization of Poly(allylamine hydrochloride) (PAH) and Poly[1-[4-(3-carboxy-4 hydroxyphenylazo) benzene sulfonamido]-1,2-ethanediyl, sodium salt] (PAZO) in Layer-by-Layer Films using Vacuum Photoabsorption Spectroscopy. *Langmuir* **2013**, *29*, 448–455. [CrossRef]
26. Ferreira, Q.; Gomes, P.J.; Raposo, M.; Giacometti, J.A.; Oliveira Jr, O.N.; Ribeiro, P.A. Influence of Ionic Interactions on the Photoinduced Birefringence of Poly [1-[4-(3-Carboxy-4 Hydroxyphenylazo) Benzene Sulfonamido]-1,2-Ethanediyl, Sodium Salt] Films. *J. Nanosci. Nanotechnol.* **2007**, *7*, 2659–2666. [CrossRef]
27. Ferreira, Q.; Gomes, P.J.; Maneira MJ, P.; Ribeiro, P.A.; Raposo, M. Mechanisms of Adsorption of an Azo- polyelectrolyte onto Layer-by-Layer Films. *Sens. Actuators B Chem.* **2007**, *126*, 311–317. [CrossRef]
28. Sério, S.; Melo Jorge, M.E.; Maneira, M.J.P.; Nunes, Y. Influence of O_2 Partial Pressure on the Growth of Nanostructured Anatase Phase TiO_2 Thin Films Prepared by DC Reactive Magnetron Sputtering. *Mater. Chem. Phys.* **2011**, *126*, 73–81. [CrossRef]
29. Siopa, D.; Sério, S.; Jorge, M.E.M.; Viana, A.S.; Gomes, A. ZnO seed layers prepared by DC reactive magnetron sputtering to be applied as electrodeposition substrates. *J. Electrochem. Soc.* **2016**, *163*, H697–H704. [CrossRef]
30. Das, S.; Pandey, D.; Thomas, J.; Roy, T. The role of graphene and other 2D materials in solar photovoltaics. *Adv. Mater.* **2019**, *31*, 1802722. [CrossRef]
31. Carreira, D.; Ribeiro, P.; Raposo, M.; Sério, S. Development of Hybrid Solar Cells based on TiO_2 or ZnO-Graphene Oxide Heterojunctions. In Proceedings of the 8th International Conference on Photonics, Optics and Laser Technology—Volume 1: PHOTOPTICS, Valletta, Malta, 27–29 February 2020; pp. 185–191, ISBN 978-989-758-401-5.
32. Krogman, K.C.; Zacharia, N.S.; Schroeder, S.; Hammond, P.T. Automated process for improved uniformity and versatility of layer-by-layer deposition. *Langmuir* **2007**, *23*, 3137–3141. [CrossRef]
33. Magro, C.; Mateus, E.P.; Paz-Garcia, J.M.; Sério, S.; Raposo, M.; Ribeiro, A.B. Electronic Tongue Coupled to an Electrochemical Flow Reactor for Emerging Organic Contaminants Real Time Monitoring. *Sensors* **2019**, *19*, 5349. [CrossRef] [PubMed]

34. Magalhães-Mota, G.; Farinha, P.; Sério, S.; Ribeiro, P.A.; Raposo, M. Photochromic Materials Towards Energy Harvesting. In *Optics, Photonics and Laser Technology. Springer Series in Optical Sciences*; Ribeiro, P., Raposo, M., Eds.; Springer Publisher: Cham, Germany, 2018; Volume 218, pp. 223–241.
35. Maria, R. Processos de adsorção em Filmes Automontados de Poli(o-metoxianilina): Evidência de Pontes de Hidrogénio além da Interação Iónica. Ph.D. Thesis, Universidade de São Paulo, São Paulo, Brasil, 1999.
36. Topsakal, M.; Ciraci, S. Effects of Charging and Electric Field on Graphene Oxide. *J. Phys. Chem. C* **2013**, *117*, 5943–5952. [CrossRef]